Updated Stagnation Point Aeroheating Correlations for Mars Entry

Thomas K. West IV*
NASA Langley Research Center, Hampton, VA, 23681

A. M. Brandis†
AMA at NASA Ames Research Center, Mountain View, CA, 94035

The objective of this work was to develop new engineering correlations for stagnation point aeroheating for Mars entry vehicles. New convective and radiative heating relations have been formulated over a wide range of entry conditions. These relations have been formulated using information from recent experimental testing and modeling enhancements. The new correlations are compared to existing relations commonly used in engineering design and analysis. Finally the correlations are tested by applying them to the Mars Pathfinder entry trajectory to demonstrate their applicability. These new correlations are a significant improvement over existing relations in terms of the accuracy, domain of applicability, and the captured physics.

Nomenclature

h	Enthalpy (J/kg-K)	μ	Dynamic Viscosity (Pa s)
Le	Lewis Number	Subscripts	
p	Pressure (Pa)	D	Dissociation
$\dot{q}_c$	Convective Heat Flux (W/cm^2)	e	Boundary Layer Edge Condition
$\dot{q}_r$	Radiative Heat Flux (W/cm^2)	eq	Equilibrium Value
R_n	Effective Nose Radius (m)	w	Wall Condition
V	Velocity (km/s)	∞	Freestream Condition
ρ	Density (kg/m^3)		

I. Introduction

As NASA progresses towards the exploration of Mars, vehicle design and concept evaluation efforts have increased significantly in the last decade. Current aeroheating engineering design practice is to use approaches that have been the same since the Apollo program. Much of this previous work made assumptions regarding the physics that were either necessary due to a lack of computing power, or simply a result of not having enough information. One example is the assumption of thermochemical equilibrium. . Recent experimental work by Brandis et al.[1] investigated the impact of non-equilibrium radiation for Mars entry conditions, which highlighted its impact. Furthermore, the impact of certain physics was not yet fully understood, such as the impact of CO_2 radiation at speeds well below what was believed to be of concern in the past.[2,3] With significant advancements in experimental testing, computers, and algorithms since then, understanding of physical processes have greatly improved. However, much of this effort has not progressed into engineering design. Previous work by Brandis and Johnston[4] evaluated the accuracy of existing heating correlations and generated new relations for Earth entry. This work aims to do provide a similar update for Mars entry. The objective of this work is to develop new convective and radiative stagnation point heating correlations for Mars entry.

*Aerospace Engineer, Vehicle Analysis Branch, Systems Analysis and Concepts Directorate, Member AIAA.
†Senior Research Scientist, Aerothermodynamics Branch, Associate Fellow AIAA.

The following section describes the existing relations for convective and radiative heating. Section III details the computational modeling approached used to generate the predictions for creating new correlations and a summary of the predictions on the domain of interest. Section IV details the new correlations and discusses their accuracy. The last section outlines key conclusions from this work.

II. Existing Relations

This section presents the existing convective and radiative heating correlations commonly used in engineering design today. A brief discussion of their applicability and limitations is also provided for each relation.

A. Convective Heating

Previous work by Lee in 1956[5] and Fay and Riddell in 1958[6] are the foundational works for correlations of stagnation point convective heating for blunt bodies at hypervelocity speeds. Both are based on the solution of the laminar boundary equations via similarity solution and numerical approximation. While Lee laid the foundation, the most notable and oft-used relation in engineering design is the one given by Fay and Riddell, shown in Eq. (1) at the stagnation point.

$$\dot{q}_c = 0.76 Pr^{-0.6} (\rho_w \mu_w)^{0.1} (\rho_e \mu_e)^{0.4} \left(1 + (Le^{0.52} - 1)(h_D/h_e)\right) (h_e - h_w)(1/R_n)\sqrt{2(p_e - p_\infty)/\rho_e} \quad (1)$$

Here, Pr is the Prandtl number, ρ is the density, μ is the dynamic viscosity, Le is the Lewis number, h is the enthalpy, h_D is the dissociation enthalpy per unit mass at the boundary layer edge, R_n is the effective nose radius, and p is the pressure. The subscripts w and e denote the wall and boundary layer edge conditions, respectively. The Lewis number, or the ratio of energy transported through conduction to energy transported by diffusion is a critical parameter. As Fay and Riddell note, if the heat transfer is to be known more exactly, the Lewis number should be calculated based on the flow properties, as opposed to using the classical unity assumption.

Another notable correlation is the one by Sutton and Graves from 1971.[7] This correlation, shown in Eq. (2) for a 97% CO_2, 3% N_2 gas, is a general relation for calculating the convective heating to the stagnation point of a blunt, axisymmetric body for gas mixtures in chemical equilibrium. An attractive feature of the Sutton-Graves correlation is its ease of implementation and is frequently used in preliminary trajectory simulations.

$$\dot{q}_c = 1.83\text{x}10^{-4} \sqrt{\rho/R_n}\, V^3 \quad (2)$$

Here, ρ is the freestream density, R_n is the effective nose radius, and V is the freestream velocity. Both of these relations provide relatively accurate predictions of stagnation point convective heating. However, both made assumptions, that today, can be relaxed, and updated gas property data are available to provide a better prediction of the physics with a computational fluid dynamics model.

B. Radiative Heating

For CO_2/N_2 environments, there have been very few radiative heating relations constructed for broad use in engineering design. The most notable is the work by Tauber and Sutton in 1991,[8] which was based on the tables from Hartung et al.[9] in 1990. Their relation, shown in Eq. (3), was built assuming a 97% CO_2 and 3% N_2 by mass atmosphere and covered a velocity range from 6.5 to 9.0 km/s. Freestream density ranged from 10^{-4} to 10^{-3} and a effective nose radius from 1 to 23 m.

$$\dot{q}_r = 2.35\text{x}10^4\ R_n^{0.526}\ \rho^{1.19}\ f(V) \quad (3)$$

In this relation, R_n is the effective nose radius, ρ is the freestream density, and $f(V)$ are tabulated values that are functions of velocity. This relation was found to be within about ±20-30% when used within its range of applicability. There were a few notable assumptions made in the radiation modeling used for this correlation. First is the assumption of thermochemical equilibrium. Recent work has show that this assumption may have a significant impact on the predicted radiation, particularly at entry speeds greater than 6 km/s.[1,10]

Other assumptions include an inviscid flow field and only the stagnation streamline was solved, however, these assumption likely have minimal impact on stagnation point radiation predictions.

A key issue with this correlation is the range of applicability. 20+ years ago, the impact of CO_2 radiation at speeds below 6 km/s was believed to have minimal heating impact or was not known to exist. The equilibrium assumption predicts too much CO_2 dissociation below 5 km/s, which results in negligible CO_2 IR radiation. Today, however, extensive testing and advances in CFD have shown that the low speed regime can have significant impact on heating due to strong emission from the CO_2 IR band system at speeds as low as 2 km/s.[2] As NASA explores new missions and opportunities at Mars, a re-evaluation of this relation is needed to include more than 20 years of recent developments and extend the applicable range of such a relation.

III. Computational Approach and Analysis

This section outlines the computational modeling approached used to create the training data for the new correlations. The domain of applicability is also discussed. Lastly, a summary of the results from the computational model is given along with a discussion of key physical features and trends of the heating.

A. Predictive Models

In this study, the flow field was modeled using the LAURA finite-volume, Navier-Stokes flow solver.[11] This solver uses a second-order, upwind, discretization scheme with Roe's flux-difference splitting scheme and Yee's Symmetric Total Variation Diminishing (STVD) formulation of the inviscid flux. For all cases, the flow field was assumed to be steady state with a two-temperature, thermochemical nonequilibrium model.[12,13] The Mars atmosphere was modeled as 97% CO_2 and 3% N_2 by mass, while the flow field was modeled using a 15 species composition model: CO_2, CO, N_2, O_2, NO, C, N, O, CN, CO^+, NO^+, C^+, O^+, N^+, e^-. The reaction finite rate chemistry model that was used is given by Johnston and Brandis.[14] This model was tuned to match CO 4^+ and CN Violet emission measured in EAST shock-tube experiments.

The boundary layer was modeled as entirely laminar as only the stagnation point is of interest in this study. The body surface was assumed to be non-ablating and in radiative equilibrium with a super-catalytic wall boundary condition. Note that the wall catalyst model on a non-ablating surface has a negligible effect on the surface radiative heating;[10] however, the super-catalytic model provides the "worst-case" for convective heating.

The radiation was modeled using the High-Temperature Aerothermodynamic Radiation (HARA) code.[15,16] In the present study, the flow field solver and the radiative heat transfer calculations are loosely coupled. A tangent-slab approximation[17] for computing the radiative flux and its divergence is used to couple the LAURA flowfield with the losses due to radiation computed by HARA. The same non-Boltzmann models and radiation properties applied by Johnston and Brandis[14] were applied here.

B. Domain of Interest

Table 1 lists the range of velocity, density, and nose radii investigated in this study. This range of conditions is representative of nearly all reasonable Mars entry conditions. The lower speed regime is covered to capture the impact of CO_2 radiation, as well as low speed convective heating. The range of effective nose radii is representative of both current and future vehicle classes, particularly the large nose radii that may be used for human exploration missions or inflatable structures. Note that effective nose radius, may differ from physical nose radius. Calibration best on historical data or testing may be necessary to determine the effective nose radius of a general vehicle shape.

Table 1: CFD conditions.

Parameter	Conditions
R_n (m)	[1, 2, 5, 10, 15, 20]
ρ (kg/m^3)	[1e-5, 5e-5, 1e-4, 5e-4, 1e-3]
Velocity (km/s)	[2.0, 2.5, 3.0, 3.5, 4.0, 4.5, 5.0, 5.5, 6.0, 6.5, 7.0, 7.5 8.0]

Results of all 390 cases are shown in Figures 1 and 2 for convective and radiative heating, respectively. There are a few interesting notes to make about these results, most notably with regards to the radiation.

First, note that the convective heating is not always the dominate heat transfer mode. As the nose radius increase, convective heating decreases (as $\sim 1/R_N^{0.5}$) and radiative heating increases (as $\sim R_N$) even above convective heat rates. Also, notice in Figure 2 that there appears to be two distinct regions of radiative heating separated at about 6 km/s. Physically, there is a switching between what molecule is most strongly emitting.

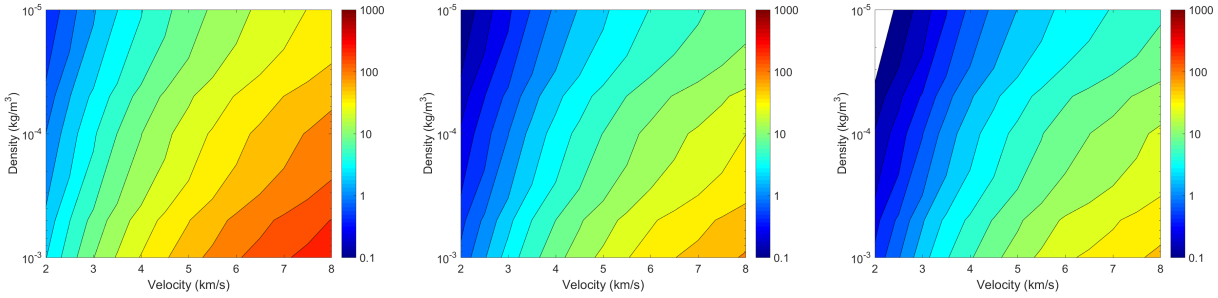

(a) $R_n = 1.0$ m. (b) $R_n = 10.0$ m. (c) $R_n = 20.0$ m.

Figure 1: LAURA/HARA predicted stagnation point convective heating (W/cm^2).

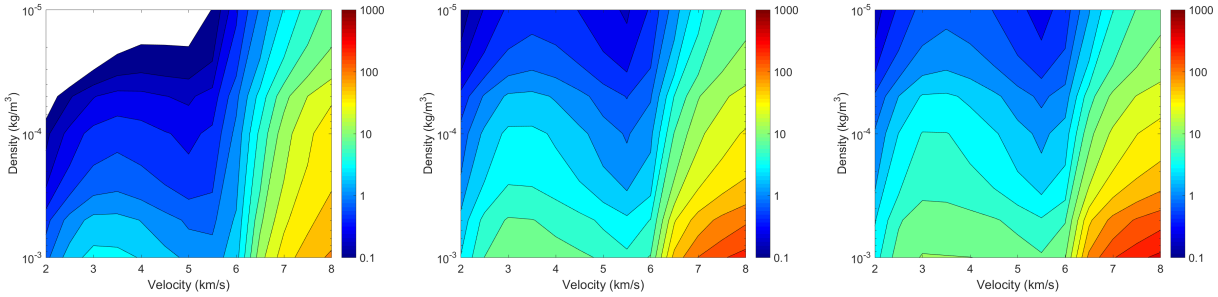

(a) $R_n = 1.0$ m. (b) $R_n = 10.0$ m. (c) $R_n = 20.0$ m.

Figure 2: LAURA/HARA predicted stagnation point radiative heating (W/cm^2).

The decrease in radiation from 8 to 6 km/s is a result of decreasing temperature due to the energy going into chemistry mechanisms. At these speeds and densities, the CO 4^+ band system emits strong vacuum ultraviolet radiation.[1] At a fixed nose radius and freestream density, the velocity dependency is illustrated in Figure 3 by comparing 6.5 km/s (Figure 3(a)) to 7.5 km/s (Figure 3(b)). Notice that increasing the velocity greatly increases the contribution from CO 4+ (6 - 8 eV) and from CN Violet (around 3.5 eV). Note that the contributions from less than about 2 eV is a mixture of other CO bands and CN Red.

The above mentioned velocity dependency is not independent of nose radius for the stagnation line. Increasing stagnation-line path length with increasing radius reduces the CO 4+ contribution through optical thickness, but increases the CN violet contribution through the increased path length for essentially optically thin emission. This is illustrated in Figure 4 by comparing nose radii of 1 and 20 m (Figures 4(a) and 4(b), respectively) at fixed freestream conditions. Additionally, notice in Figure 4 that the radiative heating at the wall does not increase significantly with nose radius at the these conditions. There is a strong flowfield-radiation coupling effect for the larger radius cases that generally reduces the peak vibration-electronic temperature behind the shock, which decreases the radiative emission.[10]

Below 6 km/s, the radiation is dominated by IR radiation from CO and, at the lower speeds, CO_2. The increase from 2 to 3 km/s is the excitation of CO_2. The subsequent decrease is the dissociation of CO_2 into CO. However, for a fixed temperature and number density, the CO IR band is a weaker emitter than the CO_2 IR band, which results in less radiation after dissociation.

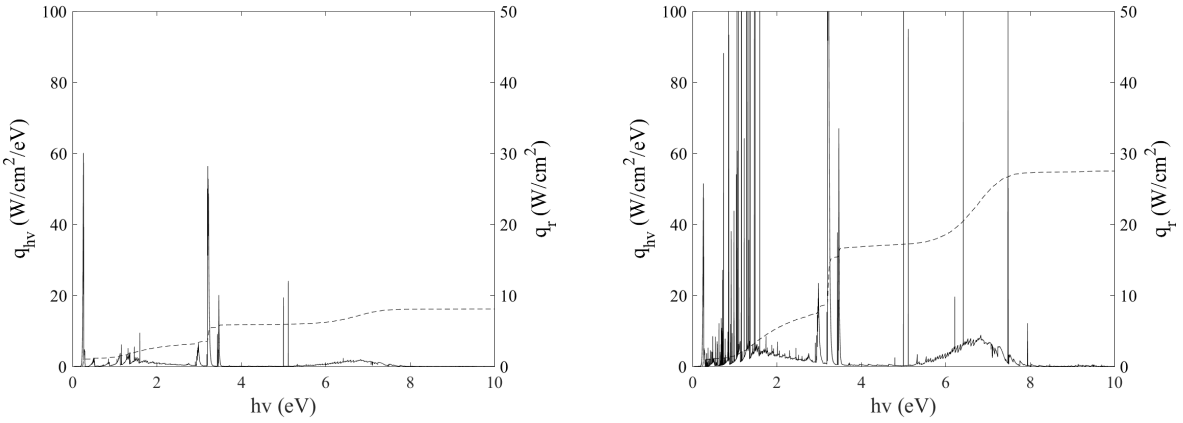

(a) $V = 6.5$ km/s. (b) $V = 7.5$ km/s.

Figure 3: High speed regime spectrum plots. R_n = 10.0 m, ρ = 1e-4 kg/m^3 .

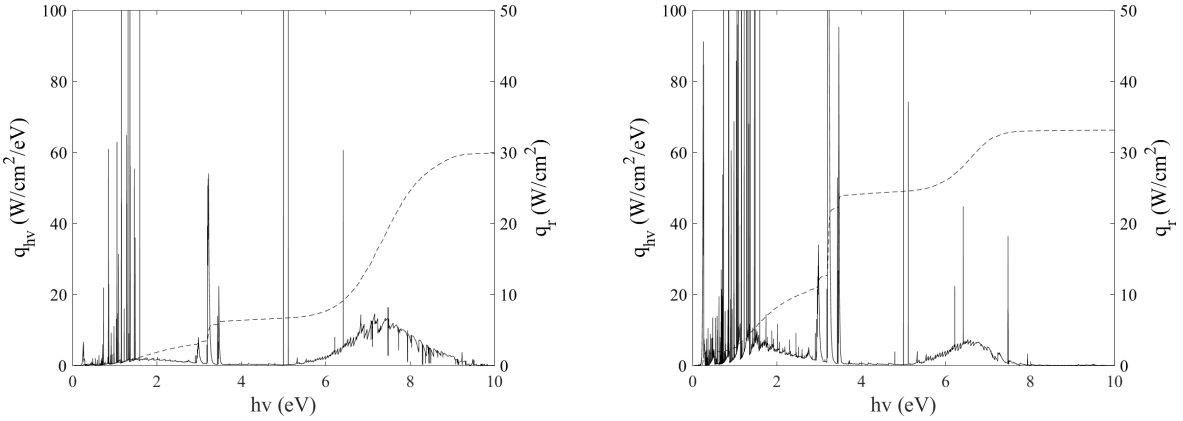

(a) $R_n = 1.0$ m. (b) $R_n = 20.0$ km/s.

Figure 4: High speed regime spectrum plots. V = 7.5 km/s, ρ = 1e-4 kg/m^3 .

IV. Updated Correlations

This section presents the new correlations created for both convective and radiative stagnation point heating predictions. Each is presented with a discussion of the functional form and the relative accuracy of the fit compared to the existing correlations discussed in the previous section. Lastly an application to Mars Pathfinder is made to demonstrate the applicability of the new correlations. This is particularly important to test how the correlations handle the tails of trajectories.

For convective heating, the same functional form as the Sutton-Graves relation has been used. Convective heating is well behaved and follows smooth trends in each of the three independent variable dimensions (freestream velocity, freestream density, and effective nose radius). The stagnation-point radiation is more complicated than the convection. Because radiation depends heavily on many factors, such shock strength, optical path length, species number densities, etc. correlations as simple as the one for convective heating are not possible. There are a significant number of interactions occurring that may be difficult to capture with simple fit forms. A second challenge unique to Mars entry, on the domain considered in this study, is the abrupt change in the radiation mechanism around 6.0 km/s (see Figure 2). Because there are two distinct physical processes occurring, fitting one global relation would result in poor accuracy. Therefore, correlations for stagnation-point radiative heating have been created in two domains of velocity.

A. Convective Heating Correlation

To generate the new convective heating correlation, shown in Eq. (4), all 390 CFD solutions were used. The same functional form as used by Sutton and Graves[7] proved to provide acceptable accuracy over more complicated forms.

$$\dot{q}_c = 7.207\ \rho^{0.47}\ R_n^{-0.54}\ V^{3.5} \tag{4}$$

Here, R_n is the effective nose radius in m, ρ is the freestream density in kg/m^3, and V is the freestream velocity in km/s. $\dot{q}_c$ is returned in W/cm^2. The accuracy of this new correlation is shown in Figure 5 for all cases above 1.0 W/cm^2 when compared to the CFD results. Notice that nearly all of the error is within ± 25% with the majority being with ± 10%. Freestream conditions of the few points around 50% error were found to be at the highest density and speeds over 7.0 km/s. While the 50% error is fairly large compared to the rest of the data, these conditions have yet to be and are unlikely to be traversed by any Mars entry vehicle.

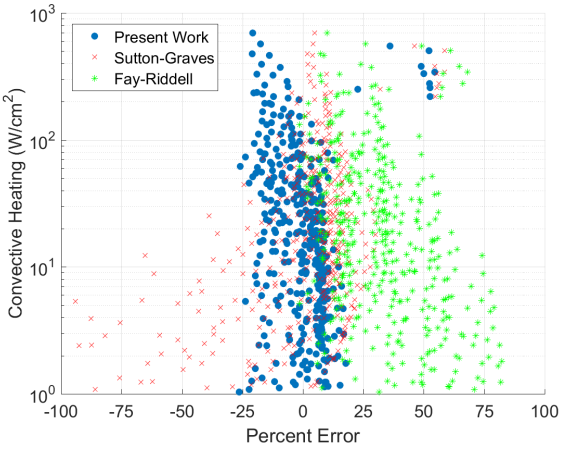

Figure 5: Comparison of convective heating predictions.

Figure 5 also compares predictions from the other two heating relations, Fay-Riddell and Sutton-Graves. The Sutton-Graves relation is well suited for higher heating cases, but the accuracy degrades as heating decreases below about 10 W/cm^2 where this correlation starts to over-predict the heating. The Fay-Riddell correlation consistently under-predicts the heating compared to the CFD values. Overall, the new correlation is a significant improvement over the broad range conditions.

B. Low-Speed Radiative Heating Correlations

To create the radiative heating fits, multiple forms were considered. Because of the significant number of interactions and the complexity of radiative heating, selection of an appropriate functional form was challenging. Therefore, two forms are presented. The first is an exponential relation based on the physics of the problem. The second is a polynomial regression of the dataset.

The exponential radiative heating correlation is given in Eq. (5). This relation applies to the full range of freestream density (1.0e-5 to 1.0e-3 kg/m^3) and effective nose radius (1 to 20 m), but only applies to freestream velocities from 2.0 km/s to at or below 6.0 km/s. The subscript eq means post-shock equilibrium. To use this relation, post-shock equilibrium flow properties must be determined. However, this calculation is very computationally inexpensive and can be easily achieved with programs such as NASA's CEA code.[18]

$$\begin{aligned}\dot{q}_r = {} & R_n^{0.5268}\ \left(0.0584\ c_{CO_{eq}}^{-0.0779}\ T_{eq}^{1.9944}\ \rho_{eq}^{0.5896}\right) \\ & + R_n^{-0.9766}\ \left(1.1778e-5\ c_{CN_{eq}}^{5.7173}\ T_{eq}^{27.4002}\rho_{eq}^{0.1826}\right) \\ & + R_n^{0.6119}\ \left(0.0022\ c_{CO_{2_{eq}}}^{1.2342}\ T_{eq}^{4.7427}\rho_{eq}^{0.4574}\right)\end{aligned} \tag{5}$$

Here, R_n is the effective nose radius and $c_{CO_{eq}}$, T_{eq}, ρ_{eq}, $c_{CN_{eq}}$, and $c_{CO_{2_{eq}}}$ are the post-shock equilibrium CO mass fraction, temperature, density, CN mass fraction, and CO_2 mass fraction, respectively. Note that these inputs are all scaled from standard SI units to help the fitting. Scale factors needed for each input are listed in Table 2. $\dot{q}_r$ returned from this correlation is in W/cm^2.

Table 2: Scale factors for the low speed radiative heating correlation.

Parameter	Base Unit	Scale Factor
R_n	m	0.1
$c_{CO_{eq}}$	-	10
$c_{CO_{2_{eq}}}$	-	10
$c_{CN_{eq}}$	-	100
T_{eq}	K	0.001
ρ_{eq}	kg/m^3	1000

A comparison of the CFD predictions to the new correlation is shown in Figure 6. Figure 6(a) shows the error for just the radiation correlation. Overall, there is a fairly large spread of the error, but is contained within about $\pm$ 25% with some under prediction occurring below 10 W/cm^2, which is contained within 50% error. While these errors appear possibly significant, the heating magnitudes are quite low, with the majority of CFD data below 10 W/cm^2. This is evident in Figure 6(b), which shows the percent error in total heating (convective and radiative) when the above correlation is used to compute the radiative heating. Convective heating is dominate for many cases in this speed regime, therefore making the error in the radiation less significant. Note that there is a comparison with the Tauber-Sutton relation. At all conditions in this speed regime, the Tauber-Sutton relation is extrapolated. As shown in Figure 6, the Tauber-Sutton relation significantly over predicts the radiative heating. In fact, these figures are truncated at -100% error, but the error for some cases can reach out over -500%. A comparison is made simply to show the significant improvement over the existing relation both in terms of accuracy and domain of applicability.

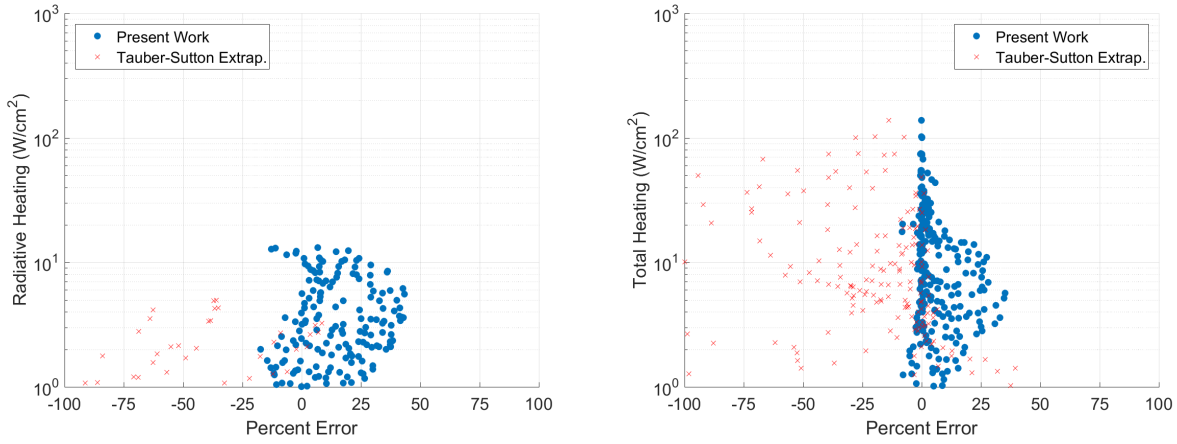

(a) Radiative heating error.

(b) Total heating error.

Figure 6: Comparison of low velocity radiative heating predictions.

As mentioned above, one caveat to using the above relation is the need to obtain the equilibrium properties behind the shock. An exponential relation, similar to the convective heating form or the Tauber-Sutton relation, that is a function of the freestream values, proved to have very poor accuracy because of the wide domain. However, using a high-order polynomial regression of the data provides a very accurate relation. This new relation is given in Eq. (6). Note that this form is fit over the same domain as the fit in Eq. (5) (freestream density of 1.0e-5 to 1.0e-3 kg/m^3, effective nose radius from 1 to 20 m, and freestream velocities from 2.0 to 6.0 km/s).

$$\dot{q}_r = e^{f(V,\rho,R_n)} \tag{6}$$

Here, $f(V, \rho, R_n)$ is a fourth-order polynomial and is a function of freestream velocity, freestream density, and effective nose radius in km/s, kg/m^3, and m, respectively. A full, fourth-order expansion of three variables

has 35 terms. The coefficients for each term are listed in Table 3. Note that several attempts were made to simplify this expression including a lower-order fit and reducing the basis of the polynomial, but each resulted in an unacceptable loss of accuracy for only slightly reduced complexity. Additionally, when using a higher order polynomial, concerns of over-fitting have to be considered. Contour lines of the domain formed using the polynomial fit are shown in Figure 7 and show the domain to be smooth and free of high frequency oscillations. Additionally, cross-validation of the regression was performed to ensure the fit is not sensitive to any small, random portion of the data. Note again that this expression is only a function of freestream parameters and the effective nose radius and requires no additional analysis to obtain the resulting radiative heating.

Table 3: Low velocity radiation correlation polynomial coefficients.

Term	Coefficient	Term	Coefficient	Term	Coefficient	Term	Coefficient	Term	Coefficient
$Constant$	-2.1851	$ln(\rho)^2$	0.0674	VR_n^2	-2.7369e-03	$V^3ln(\rho)$	-6.4747e-03	$Vln(\rho)^2R_n$	2.3530E-04
V	2.7138	$ln(\rho)R_n$	-0.1056	$Vln(\rho)R_n$	0.0108	V^3R_n	-2.9409e-03	$Vln(\rho)R_n^2$	-7.4458E-04
$ln(\rho)$	0.5949	R_n^2	-0.0545	$ln(\rho)^3$	0.0114	$V^2ln(\rho)^2$	4.4518e-04	$ln(\rho)^4$	2.2040E-04
R_n	0.0400	V^3	-0.3602	$ln(\rho)^2R_n$	-3.8751e-03	$V^2ln(\rho)R_n$	2.2275e-03	$ln(\rho)^3R_n$	-2.5058E-04
V^2	0.8212	$V^2ln(\rho)$	0.0660	$ln(\rho)R_n^2$	2.5431e-03	$V^2R_n^2$	5.5876e-04	$ln(\rho)^2R_n^2$	-1.5449E-04
$Vln(\rho)$	0.1017	V^2R_n	0.0386	R_n^3	3.8852e-03	$Vln(\rho)^3$	2.5481e-04	$ln(\rho)R_n^3$	-5.8732E-05
VR_n	-0.0220	$Vln(\rho)^2$	0.0259	V^4	0.0326	VR_n^3	-2.1412e-04	R_n^4	-7.0997E-05

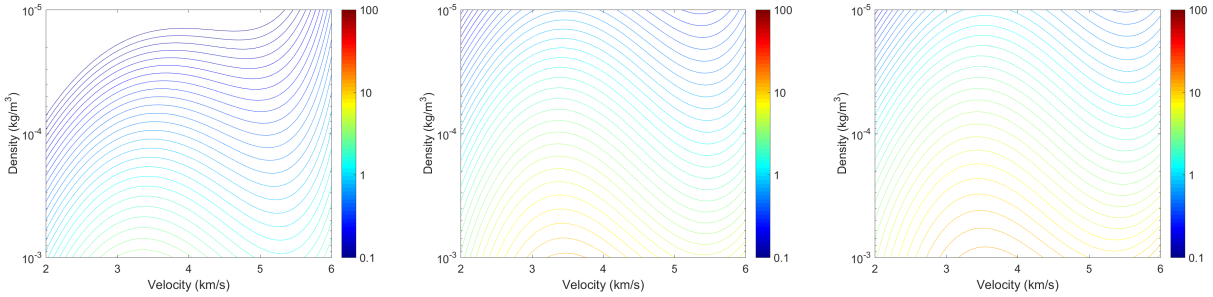

(a) $R_n = 1.0$ m. (b) $R_n = 10.0$ m. (c) $R_n = 20.0$ m.

Figure 7: Contour lines of low velocity radiative heating polynomial correlation (W/cm^2).

In comparison of the exponential fit, which is grounded more in the physics of the problem and uses less than half the number of coefficients (Eq. (5)), the polynomial proves to be a superior fit. A scatter of the error is shown in Figure 8. The error with respect to the CFD value is shown in Figure 8(a) and a comparison with the total heating is shown in Figure 8(b). The polynomial regression is in much better agreement with the training data.

There is one caveat to the polynomial form that should be considered. Engineering correlations are known for being used outside the domain of information used to train the fit. The exponential fit in Eq. (5) will tend to zero away from the training domain. Polynomials can behave erratically when extrapolated. Nonphysical or misleading results could be produced. Particular caution should be given when using the polynomial fit outside the domain of applicability.

C. High-Speed Radiative Heating Correlations

The new correlation for freestream velocities above 6.0 km/s is shown in Eq. (7). This relation has a similar form as the low speed fit.

$$\begin{aligned}\dot{q}_r = {} & R_n^{-0.0971}\left(2.0596\ c_{CO_{eq}}^{-3.2249}\ T_{eq}^{2.9479}\ \rho_{eq}^{0.2759}\right) \\ & + R_n^{0.0252}\left(0.0144\ c_{CN_{eq}}^{2.02419}\ T_{eq}^{7.8299}\rho_{eq}^{-0.3193}\right) \\ & + R_n^{0.8788}\left(0.0002\ c_{CO_{2_{eq}}}^{-0.7813}\ T_{eq}^{1.5024}\rho_{eq}^{1.5223}\right)\end{aligned} \tag{7}$$

Here, R_n is the effective nose radius and $c_{CO_{eq}}$, T_{eq}, ρ_{eq}, $c_{CN_{eq}}$, and $c_{CO_{2_{eq}}}$ are the post-shock equilibrium CO mass fraction, temperature, density, CN mass fraction, and CO_2 mass fraction, respectively. As with the

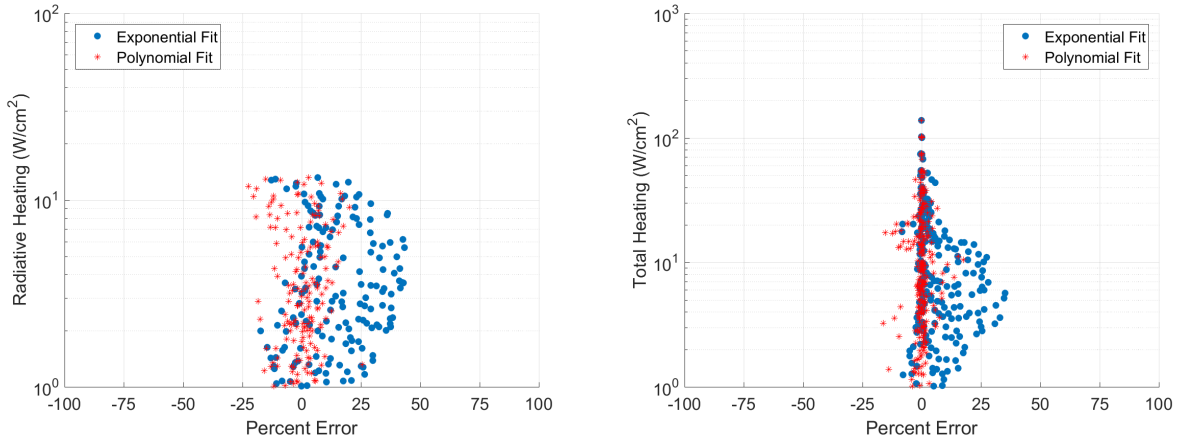

(a) Radiative heating error.

(b) Total heating error.

Figure 8: Comparison of low velocity radiative heating correlations.

low speed fit, the inputs are all scaled from standard SI units to help the fitting. The scale factors needed for each input are listed in Table 4. $\dot{q}_r$ returned from this correlation is in W/cm^2.

Table 4: Scale factors for the high speed radiative heating correlation.

Parameter	Base Unit	Scale Factor
R_n	m	0.1
$c_{CO_{eq}}$	-	10
$c_{CO_{2_{eq}}}$	-	10
$c_{CN_{eq}}$	-	100
T_{eq}	K	0.001
ρ_{eq}	kg/m^3	1000

A comparison of the CFD values with the new correlation is shown in Figure 9. The error for just the radiative heating correlation is shown in Figure 9(a). This new correlation accurately predicts the CFD values within about $\pm$ 25% for the majority of the data. There are a few outliers around 50% error. The error in the total heating when using the new correlation is shown in Figure 9(b), which shows an even better agreement with the CFD results. Similar to the low-speed relation, when cases with higher convective heating are added to low radiative heating, the error become less significant due to the relative contribution to the overall heating. Figure 9 also shows the results compared to the Tauber-Sutton relation, both on its domain of applicability and extrapolated for cases outside that domain. Consistently, the new relation is an improvement over the Tauber-Sutton relation, and has a much wider range of applicability.

Similar to the low-velocity domain, a polynomial fit of the high-velocity domain was generated to eliminate the need to obtain equilibrium values necessary for the exponential fit. This regression is shown in Eq. (8). This fit applies to the same domain as the exponential fit.

$$\dot{q}_r = e^{f(V,\rho,R_n)} \tag{8}$$

Here, $f(V, \rho, R_n)$ is a fourth-order polynomial and is a function of freestream velocity, freestream density, and effective nose radius. Again a full, fourth-order expansion of three variables has 35 terms. The coefficients for each term are listed in Table 5. As with the low-velocity fit, several attempts were made to simplify this expression including a lower-order fit and removing the dependency of one or more of the independent parameters, but each resulted in an unacceptable loss of accuracy.

To ensure over-fitting was not an issue, contours of the radiative heating produced by the polynomial fit are shown in Figure 10, which reveals no high frequency oscillations. The same cross-validation approach was used to ensure the fit is not highly dependent on any small, random portion of the dataset.

A comparison of the exponential fit (Eq. (7)) and the polynomial fit are shown in Figure 11 with the error in only radiative heating shown in Figure 11(a) and the error in total heating shown in Figure 11(b). As

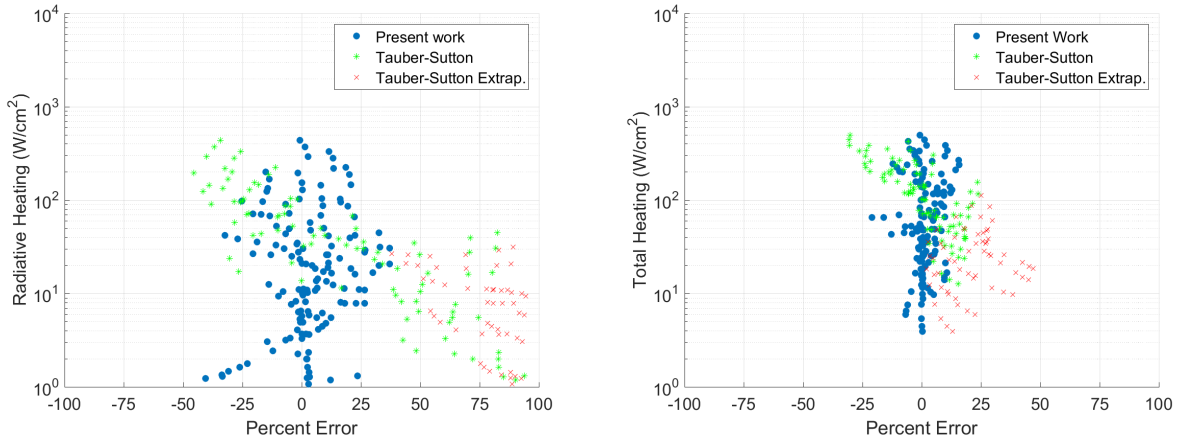

(a) Radiative heating error.

(b) Total heating error.

Figure 9: Comparison of high velocity radiative heating predictions.

Table 5: High velocity radiation correlation polynomial coefficients.

Term	Coefficient	Term	Coefficient	Term	Coefficient	Term	Coefficient	Term	Coefficient
$Constant$	-776.1295	$ln(\rho)^2$	-0.8472	VR_n^2	-7.7139e-3	$V^3ln(\rho)$	0.1704	$Vln(\rho)^2R_n$	2.9523e-3
V	327.0352	$ln(\rho)R_n$	-0.2324	$Vln(\rho)R_n$	0.0310	V^3R_n	0.0125	$Vln(\rho)R_n^2$	1.9937e-4
$ln(\rho)$	-69.4125	R_n^2	-0.0615	$ln(\rho)^3$	-0.0352	$V^2ln(\rho)^2$	3.8018e-3	$ln(\rho)^4$	1.6924e-4
R_n	-4.8702	V^3	2.5044	$ln(\rho)^2R_n$	-0.0385	$V^2ln(\rho)R_n$	1.3922e-3	$ln(\rho)^3R_n$	-1.2821e-3
V^2	-46.6552	$V^2ln(\rho)$	-3.6385	$ln(\rho)R_n^2$	-0.0155	$V^2R_n^2$	7.4385e-4	$ln(\rho)^2R_n^2$	-6.1914e-4
$Vln(\rho)$	28.0329	V^2R_n	-0.2701	R_n^3	6.8871e-4	$Vln(\rho)^3$	9.9250e-3	$ln(\rho)R_n^3$	5.8098e-5
VR_n	2.1226	$Vln(\rho)^2$	0.2091	V^4	-0.0256	VR_n^3	-1.4599e-5	R_n^4	-1.9117e-7

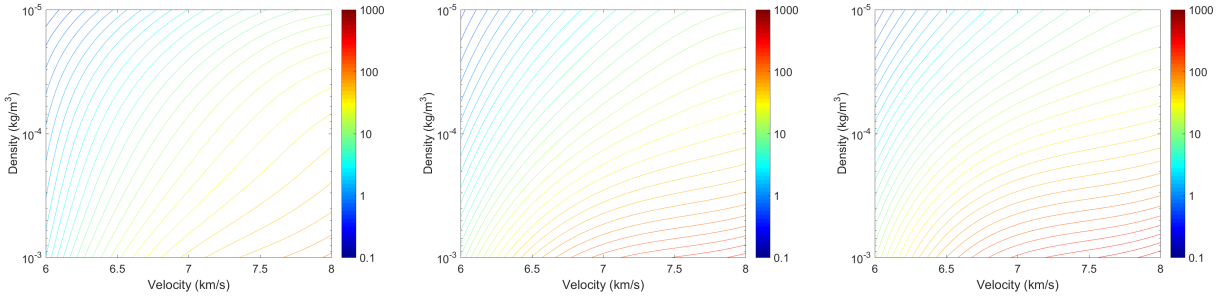

(a) $R_n = 1.0$ m.

(b) $R_n = 10.0$ m.

(c) $R_n = 20.0$ m.

Figure 10: Contour lines of high velocity radiative heating polynomial correlation (W/cm^2).

with the low-velocity fit, the polynomial regression appears to perform slightly better than the exponential fit when compared to the CFD predicted radiative heating values.

D. Application to Mars Pathfinder

The new correlations can now be applied to an example problem to demonstrate their applicability. The Mars Pathfinder trajectory entered the Martian atmosphere at about 7.5 km/s. The heatshield was a 3.5 m diameter, 70 deg. sphere-cone with about a 0.9 m nose cap radius. To run the analysis with the above correlations, an effective nose radius is needed for the sphere-cone geometry. Willcockson[19] determined the peak convective heating from the reconstructed trajectory, which was found to be about 90 W/cm^2. An effective nose radius of 1.5 m gives a similar result and was used to fly the trajectory of the Pathfinder entry with the new heating correlations. Note that this effective nose radius is calibrated to the existing data. In practice, some form of calibration may be necessary based on historical data or testing to determine the

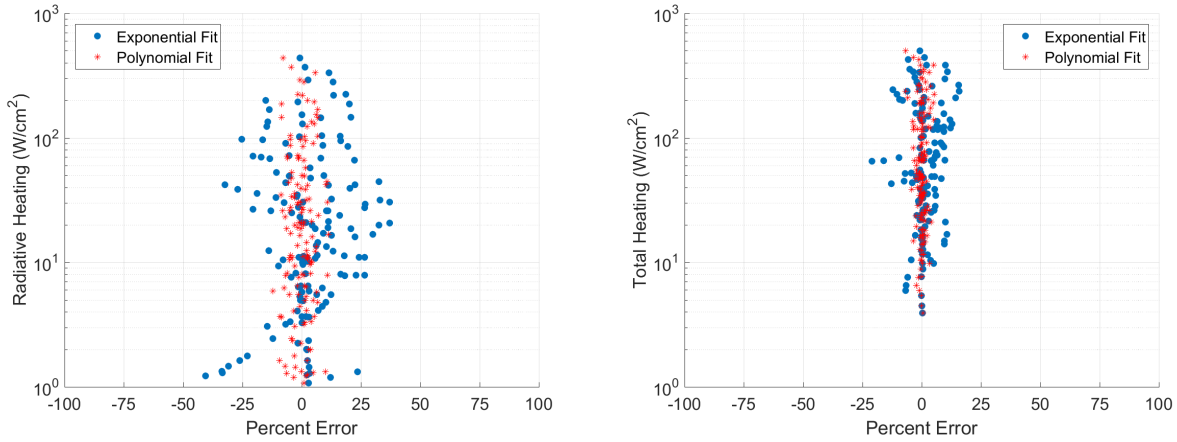

(a) Radiative heating error.

(b) Total heating error.

Figure 11: Comparison of high velocity radiative heating correlations.

correct radius. The resulting heating profiles are shown in Figure 12 in comparison to the Sutton-Graves and Tauber-Sutton relations. Figure 12(a) shows the heat flux along the trajectory and Figure 12(b).

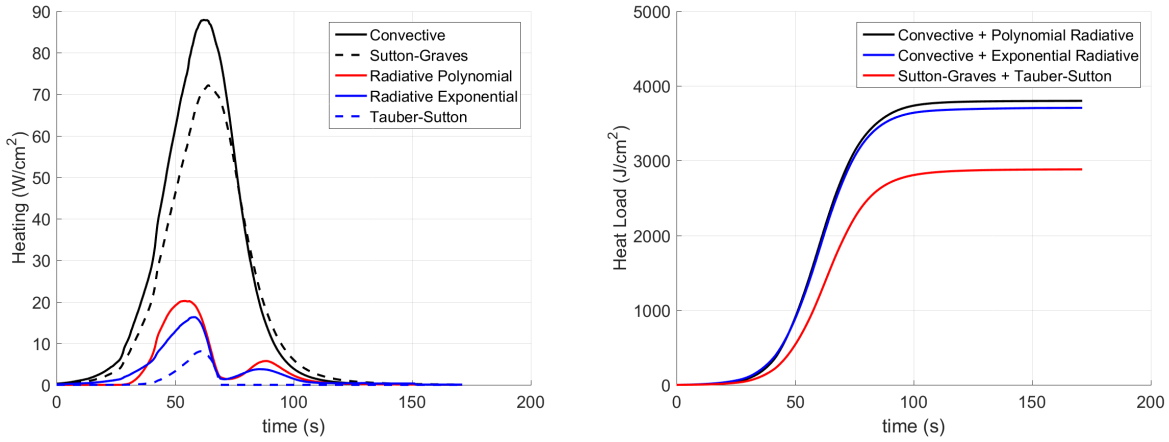

(a) Heat flux.

(b) Heat load.

Figure 12: Mars pathfinder entry heating using new correlations.

Notice there are some slight differences in the radiative heating predictions with the new correlations. Johnston et al.[10] determined that the peak radiative heating for Pathfinder was about 19 W/cm^2. The exponential and polynomial fits bound this result, which is subject to the assumption of the effective nose radius. The radiative heating profile also shows a second heat pulse, which is the result of CO_2 emission at the lower velocities. Lastly, recall that the radiative heating fits were split at 6.0 km/s. This heating profile shows a fairly smooth transition between the two, along the trajectory. In comparison to the existing correlations, the Sutton-Graves and Tauber-Sutton relations under predict the heat load by 25% for the same effective nose radius.

V. Conclusions

The objective of this work was to generate new aerodynamic heating engineering correlations for a broad range of Mars entry conditions. Significant modeling and testing improvements have been made over the last decade that have shed new light on the physical process of radiative heating there were not well understood in the past. These include nonequilibrium radiation at high velocities and CO_2 emission at low velocities

where radiation was believed to be insignificant. The new convective and radiative heating correlations were compared to existing correlations and applied to Mars Pathfinder. Overall these new relations are a significant improvement over existing relations in terms of the accuracy, domain of applicability, and the captured physics.

References

[1]Brandis, A. M., Johnston, C. O., Cruden, B. A., and Prabhu, D. K., "Investigation of Nonequilibrium Radiation for Mars Entry," AIAA Paper 2013-1055, Jan. 2013.

[2]West, T. K., Theisinger, J., Brune, A., and Johnston, C., "Backshell Radiative Heating on Human-Scale Mars Entry Vehicles," AIAA Paper 2017-4532, June 2017.

[3]Brandis, A. M., Saunders, D. A., Johnston, C. O., Cruden, B. A., and White, T. R., "Radiative Heating on the After-Body of Martian Entry Vehicles," AIAA Paper 2015-3111, Jan. 2015.

[4]Brandis, A. M. and Johnston, C. O., "Characterization of Stagnation-Point Heat Flux for Earth Entry," AIAA Paper 2014-2374, June 2014.

[5]Lees, L., "Laminar Heat Transfer Over Blunt-Nosed Bodies at Hypersonic Flight Speeds," *Jet Propulsion*, Vol. 26, No. 4, 1956, pp. 259–269.

[6]Fay, J. A. and Riddell, F. R., "Theory of stagnation point heat transfer in dissociated air," *Journal of Aeronautical Sciences*, Vol. 25, No. 2, 1958, pp. 73–85.

[7]Sutton, K. and Graves Jr., R. A., "A General Stagnation-Point Convective-Heating Equation for Arbitrary Gas Mixtures," Tech. Rep. NASA TR R-376, Nov. 1971.

[8]Tauber, M. E. and Sutton, K., "Stagnation-Point Radiative Heating Relations for Earth and Mars Entries," *Journal of Spacecraft and Rockets*, Vol. 28, No. 1, 1991, pp. 40–42.

[9]Hartung, L. C., Sutton, K., and Brauns, F., "Equilibrium radiative heating tables for aerobraking in the Martian atmosphere," Tech. Rep. NASA TM-102659, May 1990.

[10]Johnston, C. O., Brandis, A. M., , and Sutton, K., "Shock Layer Radiation Modeling and Uncertainty for Mars Entry, AIAA 2012-2866," 43^{rd} *AIAA Thermophysics Conference*, New Orleans, LA, June 2012.

[11]Mazaheri, A., Gnoffo, P. A., Johnston, C. O., and Kleb, B., "LAURA Users Manual: 5.5-64987," Tech. rep., NASA/TM-2013-217800, Feb. 2013.

[12]Gnoffo, P. A., Gupta, R. N., and Shinn, J. L., "Conservation Equations and Physical Models for Hypersonic Air Flows in Thermal and Chemical Nonequilibrium," Tech. rep., NASA TP 2867, Feb. 1989.

[13]Park, C., Howe, J. T., Jaffe, R. L., and Candle, G. V., "Review of Chemical-Kinetic Problems for Future NASA Missions, II: Mars Entries," *Journal of Thermophysics and Heat Transfer*, Vol. 8, No. 1, 1994, pp. 9–23.

[14]Johnston, C. O. and Brandis, A. M., "Modeling of nonequilibrium CO Fourth-Positive and CN Violet emission in CO_2 - N_2 gases," *Journal of Quantitative Spectroscopy and Radiative Transfer*, Vol. 149, No. 1, 2014, pp. 303–317.

[15]Johnson, C. O., Hollis, B. R., and Sutton, K., "Spectrum Modeling for Air Shock-layer Radiation at Lunar-Return Conditions," *Journal of Spacecraft and Rockets*, Vol. 45, No. 5, 2008, pp. 865–878.

[16]Johnson, C. O., Hollis, B. R., and Sutton, K., "Non-Boltzman Modeling for Air Shock Layers at Lunar Return Conditions," *Journal of Spacecraft and Rockets*, Vol. 45, No. 5, 2008, pp. 879–890.

[17]Johnston, C. O., "Improved Exponential Integral Approximation for Tangent-Slab Radiation Transport," *Journal of Thermophysics and Heat Transfer*, Vol. 24, No. 3, 2010, pp. 659–661.

[18]McBride, B. and Gordon, S., "Computer Program for Calculation of Complex Chemical Equilibrium Compositions and Applications I. Analysis," Tech. Rep. NASA RP-1311, Oct. 1994.

[19]Willcockson, W. H., "Mars Pathfinder Heatshield Design and Flight Experience," *Journal of Spacecraft and Rockets*, Vol. 36, No. 3, 1999, pp. 374–379.